Journal of Zhejiang University-SCIENCE A (Applied Physics & Engineering) in press
www.jzus.zju.edu.cn; www.springer.com/journal/11582
E-mail: jzus_a@zju.edu.cn

Research Article

https://doi.org/10.1631/jzus.A2300449

Design of a 35-kV high-temperature superconducting synchronous machine with optimized field winding

Chao LUO[1], Bowen XU[1], Jien MA[1]✉, Jiancheng ZHANG[2], Jiabo SHOU[1], Youtong FANG[1]

[1]*College of Electrical Engineering, Zhejiang University, Hangzhou 310027, China*
[2]*Electric Power Research Institute of State Grid Zhejiang Electric Power Corporation, Hang Zhou 310014, China*

Abstract: This paper proposes the application of high-voltage stator-cable windings in superconducting machines, based on the characteristics of strong magnetic fields and large air gaps. Cross-linked polyethylene cable winding can be employed to achieve a rated voltage of 35 kV in DC-field superconducting machines, thereby enabling a direct connection between the superconducting machine and the power grid, eliminating the need for transformers. We first, through finite-element analysis, demonstrate that the proposed high-voltage high-temperature superconducting machine not only meets the requirement of a 35-kV rated voltage, but also exhibits minimal flux leakage, torque fluctuation, and harmonic distortion. We then compare three candidate Types to discuss the tradeoff between the multi-group superconducting field winding arrangement and machine performances. We propose inverted trapezoidal superconducting field winding as a promising candidate, because it has minimal superconductivity material usage, the largest safety margin for the superconducting coils (SC), low thrust ripple, and low total harmonic distortion with the desired 35-kV-rated voltage. Finally, through large-scale design parameter sweeping, we show how we selected the optimal parameters for field winding and validated them by the finite-element method.

Key words: High voltage stator-cable windings; superconducting machines; inverted trapezoidal field winding; total harmonic distortion

1 Introduction

In recent years, superconducting machines have been regarded as promising new equipment for industrial and transportation applications, offering steady reductions in the cost of superconducting materials and continuous improvements in their performance (Qiuli, 2022) (Muttaqi et al., 2019) (Masson and Luongo, 2005) (Cucciniello et al., 2022). They exhibit remarkable benefits such as compact structure, superior efficiency, and high torque density (Terao et al., 2019) (Dias et al., 2022). These characteristics have made them a standard solution for space-sensitive applications such as offshore platforms (Hsieh et al., 2013) (Wang et al., 2015) (Fang et al., 2015).

Superconducting machines can be divided into two primary categories: fully superconducting machines(Balachandran et al., 2022) (Kovalev et al., 2019) (Manolopoulos et al., 2020) (Liu et al., 2021) and direct-current (DC) -field superconducting machines. The development of fully superconducting machines is currently confined to the realm of theoretical research (Komiya et al., 2020). Superconducting machines are largely commercialized as DC-field Types, in which DC-field excited superconducting windings are employed in the rotor and traditional copper windings are adopted for the stator. During the era of low-temperature superconductivity (LTS), these machines demonstrated their reliability, with a 70 MW LTS motor in Japan running stably for 1500 hours with a rated voltage of 10 kV (Oishi and Nishijima, 2002). In 2019, Bong et al. outlined a design investigation into a 40-MW synchronous motor featuring no-insulation (NI) HTS field windings (Bong et al., 2019). The rated voltage of 6.6 kV

✉ Jien MA, majien@zju.edu.cn
Jien MA, https://orcid.org/0000-0003-0756-1508

Received Sept. 1, 2023; Revision accepted Dec. 20, 2023;
Crosschecked

indicated a high rated current. A 10-MW fully superconducting generator with HTS superconducting tapes was studied by Komiya et al. in 2019. The rated voltage of the motor was 6.9 kV. The China Southern Power Grid Corporation proposed the electromagnetic design for a 10 Mvar DC-field HTS synchronous condenser in 2021 (Duan et al., 2022). The rated voltage of this motor was 11 kV, which meant that it needed to be connected to the grid with a transformer to adjust the reactive power. In the above examples, the power density of the machines was significantly improved by employing high-current-density superconducting field windings. However, almost all DC-field superconducting machines are conventional machines with the addition of superconducting rotors. The full potential advantages of superconducting machines remain underutilized, thus limiting the widespread adoption and implementation of DC-field superconducting machines. Moreover, the majority of DC-field superconducting machines have voltage ratings below 13.8 kV, necessitating their connection to the grid through a transformer.

In order to further improve the power density of superconducting machine systems, the primary objective of this study was to investigate superconducting machines that can be directly connected to the grid to further increase the power density of the system. Superconducting machines offer excellent advantages over traditional room-temperature high-voltage machines (Liu et al., 2022) (Sumption et al., 2020), including a remarkably high magnetic field and non-magnetic stator teeth, which cause the voltage to exhibit very low levels of total harmonic distortion (THD). This design also creates additional room to accommodate the high-voltage armature windings, enabling a substantial augmentation in the number of winding turns. Therefore, in this study, cross-linked polyethylene (XLPE) cable winding was employed to achieve a rated voltage of 35 kV in the DC-field superconducting machines, thereby enabling a direct connection between the superconducting machine and the power grid, and eliminating the need for transformers (Lee et al., 2014) (Gao et al., 2019) (Li et al., 2023). This advancement significantly enhances the short-circuit capacity and power density of the system. This paper presents a comprehensive design and optimization process for high-voltage high-temperature superconducting (HVHTS) machines. The field winding was optimized to meet the low THD of the voltage required by the grid, while minimizing the amount of superconducting tape. In addition, it was necessary to combine the properties of superconducting materials and design the structure of the superconducting magnet coil to weaken the influence of sensitive angle fields on critical current and improve the utilization efficiency of the superconducting material. Finally, an inverted trapezoidal field winding HVHTS machine was validated and appeared to be a promising candidate.

The rest of this paper is organized as follows. The structure of the HVHTS motor and the design method and theory are presented in Section II. In Section III, the electromagnetic performance of three candidates for the machine design are compared. In Section IV, the influence of several key parameters of the proposed HVHTS machine are discussed in detail. Section V concludes the paper.

2 Design of high-voltage superconducting machines

The basic design for 35 kV HTS synchronous machines employs a DC HTS field winding. An ultra-high-voltage stator using cross-linked polyethylene (XLPE) cable winding is employed to achieve a rated voltage of 35 kV. The proposed HVHTS machines incorporate a stator back iron made of laminated iron. The rotor employs four double-pancake HTS coils for the rotor field winding, and, a slotless stator and a coreless rotor are chosen. Fig. 1 shows the topology of the proposed HVHTS machine.

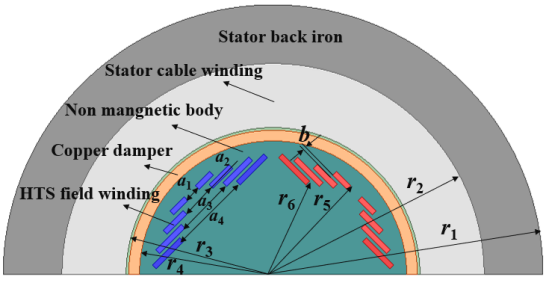

Fig. 1 Topology of a HVHTS machine

In the design of superconducting machines, critical factors such as terminal voltage and rotor speed are principally dictated by the power system. These parameters establish the design criteria for the machines. In this section, we explain the design of a DC-field HTS machine with a rated line voltage of 35 kV.

2.1 Stator design

Currently, almost all synchronous machines are designed with a limitation on their output voltage, capping it at 25 kV. Asea Brown Boveri (ABB) has successfully conducted experiments with cable insulation for high-voltage generators rated at 45 kV, and successfully connected them to the grid at the Purjus hydroelectric power station in Sweden (Perers et al., 2007). It is noteworthy that high-voltage cables equipped with XLPE insulation have now been improved further, reaching voltages of up to 500 kV (Metwally et al., 2008).

The key to designing the stator with a rated voltage of 35 kV is to determine the cable diameter. According to Hao et al. (2012), the electric field in the stator winding is distributed between the inner and outer semiconductor layers of the cable. The cable capacitance per unit length C_0 between the inner and outer semiconductor can be calculated from

$$C_0=\frac{1.778e^{-11}\pi m_1}{\ln(r_{a1}/r_{a2})}, \tag{1}$$

where relative permittivity m_1=2-3, r_{a1} is the outer radius of the inner semiconductor layer, and r_{a2} is the inner radius of the outer semiconductor layer.

However, C_0 varies at different positions along the winding as the insulation thickness of the cable increases gradually from the neutral to the terminal (Tian and Lin, 2006). As an example, we will use a two-segment cable as a model for high-voltage winding, as shown in Figure 2. The proportion between the two segments is a:(1-a). U_1 and U_2 are terms used to denote neutral voltage and terminal voltage, respectively. The capacitance per unit length for the first and second segments are represented by C_1 and C_2, respectively. The entire length of the winding is denoted as l. The voltage per unit length of phase a in the winding, represented by E_{12}, has a relationship with the neutral and terminal voltages.

$$\dot{E}_{12}\,l=\dot{U}_1-\dot{U}_2 \tag{2}$$

The capacitive current I_a of phase a during normal operation can be calculated as follows:

$$\dot{I}_a=j\omega\int_0^{al}\dot{E}_{12}\,xC_1\mathrm{d}x+j\omega\int_{al}^{1}\dot{E}_{12}\,xC_2\mathrm{d}x \tag{3}$$

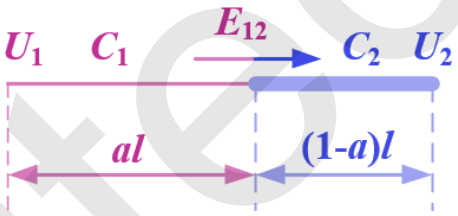

Fig. 2 The two-segment cable

Consider a high-voltage synchronous machine operating at 35 kV. The stator-cable winding of the HVHTS machine, as depicted in Fig. 3, is configured with ten cables within each slot. After the rated voltage and rated current of the motor are determined, the insulation thickness is determined iteratively according to formulas (1) - (3). This paper has simplified that the first five cables nearest to the rotor surface are rated for 10 kV, while the remaining five are 20-kV cables. The fundamental design parameters for this 35-kV stator-cable winding are provided in Table 1.

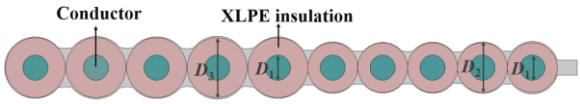

Fig. 3 Slot of a 35-kV high-voltage stator with ten cables

Table 1 Cable configuration of high-voltage stator

Parameter	value
Diameter of conductor/mm	10
Diameter of 10 kV cable/mm	20
Diameter of 20 kV cable/mm	24
10 kV cable slot width/mm	22
20 kV cable slot width/mm	26

2.2 HTS Field-winding design

In this study, for a more sinusoidal air-gap magnetic-field waveform, the rotor had four pairs of double-pancake SCs arranged in a stepped/tiered fashion. Taking into consideration the support and fixation, the cross-sectional structure of the SCs could not be allowed to exceed the rotor's virtual contour line (shown in Figure 4). By choosing a suitable air gap between the inner radius of the stator armature winding (r_3) and the radius of the rotor field winding (r_6), the total magnetomotive force (MMF) of the rotor HTS windings could be represented (Miller and Hughes, 1977) (Abrahamsen et al., 2009) (Seo et al., 2023). This representation is a function of the magnetic flux density B_s, the average radius r_b, turns of field winding N_{bf}, field current i_{bf}, poles p, and the field-winding radius r_{bf}.

$$N_{bf} i_{bf} = \frac{\pi r_f B_s}{\mu_0 (\frac{r_{bf}}{r_b})^{p+1} [1 + (\frac{r_b}{r_{bi}})^{2p}]}. \quad (4)$$

The B_s in (4) is calculated as follows:

$$B_s = \frac{\mu_0 N_{bf} i_{bf} r_{bf}}{D^2} [1 + (\frac{r_b}{r_{bi}})^2]. \quad (5)$$

Setting the cross-sectional area of each superconducting coil to A_{wire} and the total cross-sectional area of the excitation coil to A_{coil}, turns of field winding N_{bf} is:

$$N_{bf} = \frac{A_{coil}}{A_{wire}}. \quad (6)$$

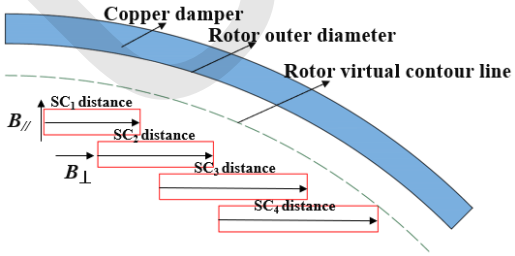

Fig. 4 Constraints on the superconducting field coils

2.3 Kim-like model for superconducting properties

The SC can only maintain superconducting properties when the incoming current is less than the critical current. Kim pointed out that the critical current density of a superconductor is not only dependent on temperature, but also on the external magnetic field. In this analysis, it is assumed that the critical current decreases most significantly due to magnetic fields perpendicular to the tape face, which allows the application of a Kim-like model (Kim et al., 1964), as in:

$$I_c(B_\perp, B_{//}) = \frac{I_{c0}}{(1 + \sqrt{kB_{//}^2 + B_\perp^2} / B_c)^\alpha}, \quad (7)$$

where I_{c0} is the critical current under the self-field of the superconducting strip, $B_\perp$ and $B_{//}$ are the magnitude of the magnetic field perpendicular and parallel to the superconducting strip, respectively, and k, α, and B_c are the parameters fitted by experimental data. Figure 5 illustrates the variation of the critical current of REBCO with respect to the parallel and perpendicular external magnetic field at 30 K. This constraint primarily influences the selection of the field current.

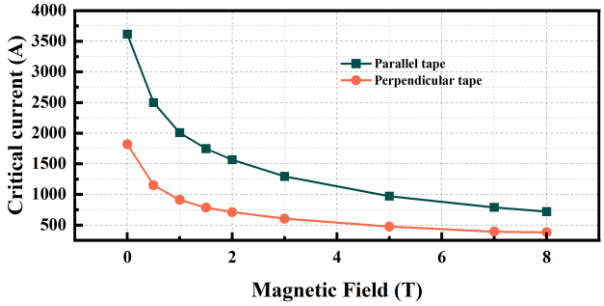

Fig. 5 Variation in critical current of HTS with magnetic field

3 Electromagnetic performance analysis

For comprehensive design and optimization of HVHTS machines, it is vital to develop a precise model. Consequently, we employed the finite-element method (FEM), as shown in Figure 6. Simulations were carried out using the full model, utilizing the Maxwell transient solver with a 0 Vec-

torPotential boundary for the outer arc of the stator back iron. To delve deeper into the influence of the stator-rotor end, we generated a 3D finite-element model (Figure 7). However, owing to the substantial computational load, the 3D finite-element calculation required 14 hours per iteration. This extended time frame was a result of predominantly utilizing a 2D finite-element approach for the optimized design. In this section, we describe the quantitative comparison of three typical Types of HVHTS machines by FEM. As can be seen in Fig.10, the three counterparts have the same stator structure. The detailed geometric parameters are listed in TABLE II. Type II and Type III rotors employ four pairs of double-pancake SCs with a trapezoidal layout, characterized by a stepwise increasing of SCs from the topmost to the lower SCs. In contrast, Type I employs an inverted trapezoidal layout, characterized by a stepwise decrease of SCs from top to bottom. Notably, Type II situates the topmost coil closer to the air gap, while Type I and Type III share a similar positioning. The number of SCs in Type III is 2026, which is 110% and 102% of the numbers in Type I and Type II.

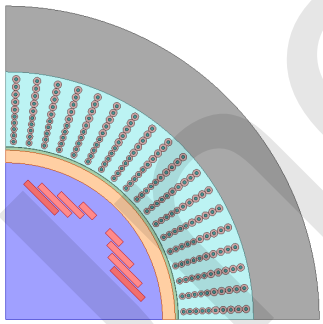

Fig. 6 1/4 2D FEM model of a 15-MW HVHTS machine

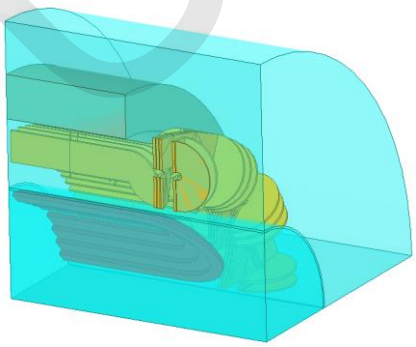

Fig. 7 1/16 3D FEM model of a 15-MW HVHTS machine

Table 2 Design parameters of Type I-Type II

Parameter	Type I	Type II	Type III
Rated voltage/kV		35	
Speed/rpm		1500	
Pole number		4	
Slot number		72	
Stator outer radius(r_1)/mm		1010	
Stator inter radius(r_2)/mm		790	
Effective length/mm		1175	
Operating current/A		480	
Damper inter radius(r_4)/mm		500	
Damper outer radius/mm		540	
Armature coil inter radius(r_3)/mm		551	
Armature coil outer radius(r_2)/mm		790	
SC width/mm		10	
SC thickness/mm		0.4	
Field coil outer radius(r_5)/mm	441	461	441
Field coil inter radius(r_6)/mm	376	394	376
Number of coils SC_1	610	340	376
Number of coils SC_2	530	490	450
Number of coils SC_3	424	560	574
Number of coils SC_4	276	600	626
Toal coil	1840	1990	2026
b pitch/mm	5	5	5
a_1 pitch/mm	60	60	60
a_2 pitch/mm	218	140	144
a_3 pitch/mm	360	240	240
a_4 pitch/mm	490	300	352

Fig. 8 shows the open-circuit phase back-EMF waveforms of the three candidates, and Fig. 8 shows the corresponding spectra. One of the main objectives of this study was to improve the voltage waveforms, which is outlined and extensively discussed in this section. It is notable that the amplitude of Type II is 3.7% higher than that of Type I. Figure 9 also shows the existence of high synchronization between the back-EMF and the corresponding spectra in Types I and III. In all three candidates, the low values of the third and fifth harmonic amplitudes demonstrated the proper design of the proposed machine. In addition, the THD of the voltage waveform was calculated to be less than 5.1%, 9.3%, and 5.3% for Types I, II, and II. The results reveal that the peak value of the phase voltage amounts to approximately 27.8 kV, while the effective value of the phase voltage reaches around 19.7 kV. Consequently, the rated three-phase voltage adequately fulfills the stipulated 35 kV requirements.

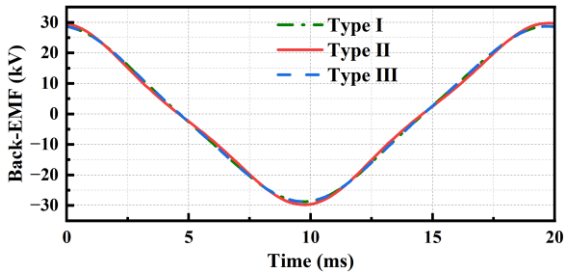

Fig. 8 Comparison of phase back-EMF waveforms

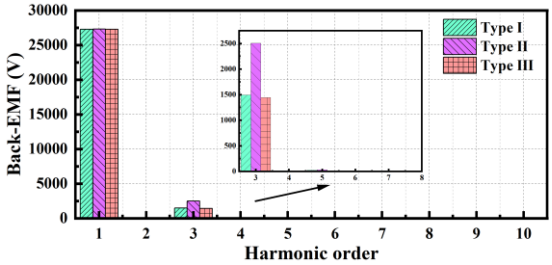

Fig. 9 Comparison of phase back-EMF spectra

It is evident from Fig.10 that the average torque for all three types is almost identical, with each type globally optimized to achieve the maximum average torque while adhering to the constraint of 4.3 kW copper loss, approximately 91.2 kNm, owing to the equal fundamental component of the magnetic field within the air gap. Upon achieving a steady state, the torque for Type II peaks at 91.38 kNm, in contrast to the minimum value of 91 kNm, resulting in a torque fluctuation of approximately 0.38 kNm. Furthermore, many peaks are apparent in the Type II curves. Compared with the torque ripple in Type II, 28.6% and 63% torque-ripple reduction is achieved for Types I and III. The results of our calculations demonstrate that when the sides of the stator are identical, Type I employs 7.5% and 9.2% fewer SCs compared to Type II and Type III, respectively. Moreover, despite this reduction, Type I can generate the same average torque with significantly lower torque ripple.

As depicted in Figure 11, the 3D finite-element analysis outcomes reveal that comparable results can be achieved. This is because the superconducting rotor end generates a robust magnetic field, causing the magnetic lines of force to interlink with the stator. Consequently, all three types of torque appear to increase when the end is taken into account. With an equivalent superconducting usage as in the 2D case, Type 1 maintains the highest average torque and the least torque fluctuation.

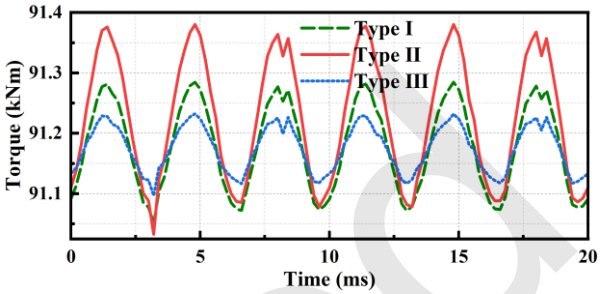

Fig. 10 Comparison of torque (2D)

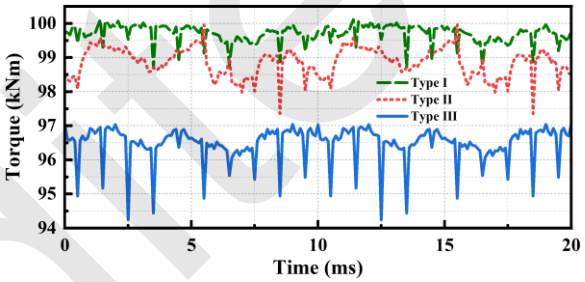

Fig. 11 Comparison of torque (3D)

Fig. 12 demonstrates the flux-density and flux-line distribution in the cross-section of the three Types of HVHTS machines. It is clear that the magnitudes of the flux density around the HTS coils are much higher than those around other parts. Moreover, the innermost regions of the SCs in all three Types experience by far the highest magnetic field. This indicates that the critical current of an SC is determined by the magnetic field in its innermost regions. Among the three Types, the SCs of Type I were subjected to the least external magnetic field at their corresponding locations. We attribute this to the fact that all three Types of SC operate at the same current density, while Type I has the fewest number of coils. Fig. 10 also reveals that the three Types have the same main flux through the center of the N-pole coil, the stator yoke, the center of the S-pole coil, and the rotor yoke, with minimal flux leakage. For all three Types, flux leakage near the air gap is minor, but the level of flux leakage between the North and South poles of the rotor and the coil is relatively high. This is attributable to the robust magnetic field created by the SCs and the considerable magnetic potential on the stator side.

This means that flux leakage does not rise significantly with the widening of the physical air gap in these HVHTS machines.

Because of the symmetry of the rotor coil, we selected only one pole for analysis (see Fig. 13), with the upper half divided into the left part of one pole in Fig. 10 and the lower half into the right part. The maximum flux density in all three Types is exhibited in the topmost SC. However, the highest flux density in Type I is predominantly parallel to the SC, whereas the flux-density components in Types II and III are considerably greater in the vertical SC. Apart from the innermost flux lines, which are nearly parallel, all others display curvilinear trajectories, creating a distinct "nucleus point" within the lower coil. Maximum flux leakage is observed in the lower coil, with the flux density at the "nucleus point" being the least.

Based on the information in the first section, the critical current of an SC at the same temperature is determined by the magnitude of the magnetic fields parallel and perpendicular to it. Therefore, we calculated the parallel and perpendicular magnetic fields near the SC in three different scenarios.

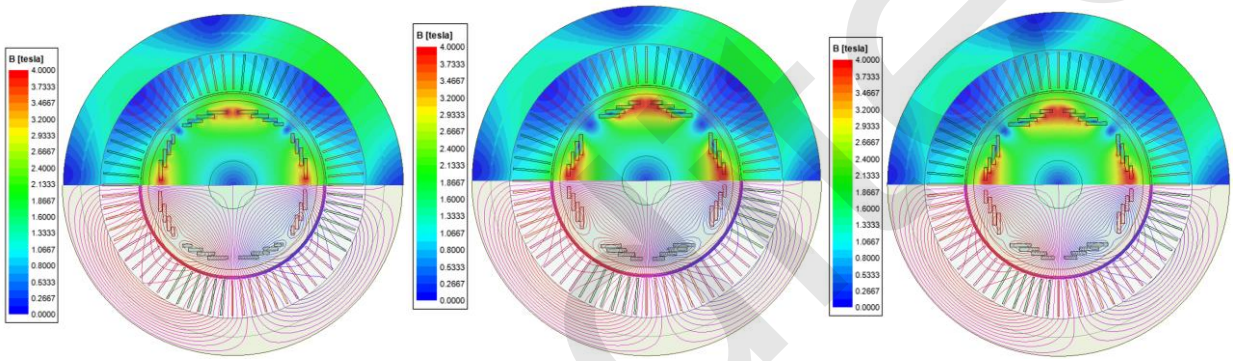

(a) (b) (c)

Fig. 12 Flux-contour distributions of three SC candidates . (a) Type I. (b) Type II. (c) Type III

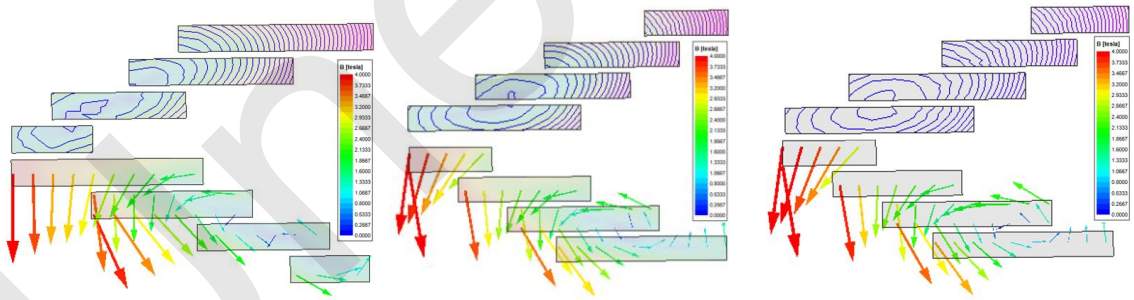

(a) (b) (c)

Fig. 13 Flux-contour distributions of the three SC candidates. (a) Type I. (b) Type II. (c) Type III

The magnetic field in the parallel SC corresponds to the results in Figs. 14 to 17. When calculating the magnetic field in parallel SC_1 and SC_2, the absolute of the magnetic field is consistently smaller for Type I compared to both Type II and Type III, despite Type I having a larger number of coils. Considering SC_3, the peak value of Type I in the external magnetic field was determined to be 1.8 T. Figure 16 represents a reduction of approximately 38.7% and 41.9% compared to Types II and III, respectively. Similarly, for SC_4, the peak value of Type I was calculated to be 0.9 T, which corresponds to 34.6% and 40.9% of the values for Types II and III, respectively.

Comparing Figures 14 to 17, it is apparent that the maximum of the magnetic field in the parallel SC for all three Types is located on the innermost side of SC_1. The maximum of Type III is 4.05T, which is 104% and 102% of the value for Types I and II. It is worth noting that all three Types exist in regions where the magnetic field of the parallel SC is zero.

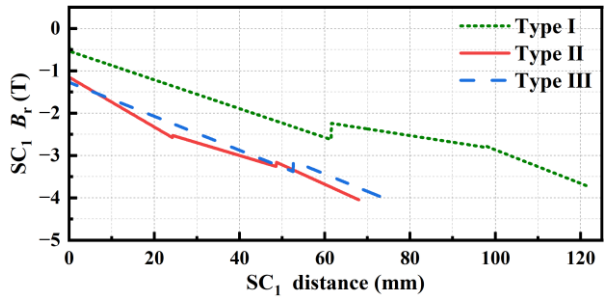

Fig. 14 Comparison of magnetic field of the parallel SC_1

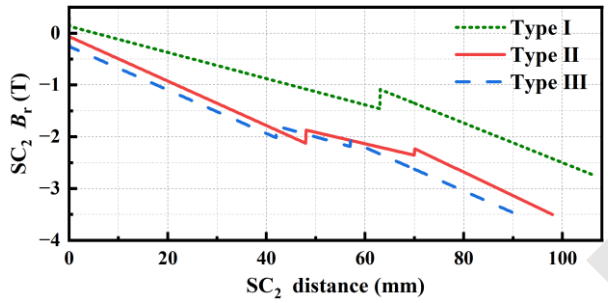

Fig. 15 Comparison of magnetic field of the parallel SC_2

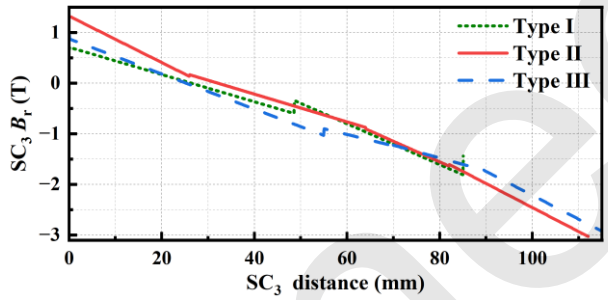

Fig. 16 Comparison of magnetic field of the parallel SC_3

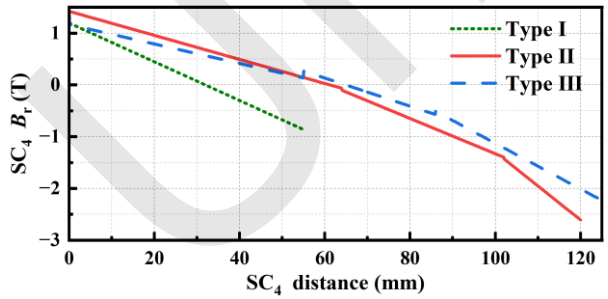

Fig. 17 Comparison of magnetic field of the parallel SC_4

The distribution of the magnetic field perpendicular to the SC corresponds to the results in Figures 18 to 21. We found that the highest perpendicular magnetic field consistently resides in the innermost region of the coil. Notably, if the SC_1 distance surpasses 60 mm, the perpendicular magnetic field of the coils maintains a consistent value of approximately -0.1T, regardless of the increasing distance from SC_1. Both Types II and III exhibited a peak value of the perpendicular magnetic field of approximately 2.6 T, located within the SC_3. Conversely, for Type I, the maximum value was slightly lower, approximately 2.4 T, also situated within the SC_3. All three Types exist in regions where the magnetic field of the perpendicular SC is zero.

It is known that the magnetic field of the perpendicular SC has a more dramatic impact on current density than the magnetic field parallel to it. However, since the magnetic field in a machine is continuously changing in terms of the impact of the magnetic field on HTS coils, it should be treated as a perpendicular field to ensure the safety of HTS coils. Because of this, the SC of Type III experienced the highest external magnetic field of all three Types, reaching a maximum of 4.1 T. Nevertheless, the SC of Type I had the lowest external magnetic field at 3.8 T, with all three Types having a field current density of 480 A. Furthermore, the field distributions within the coils are much more uniform (smaller field angles) in Type I. The variation in critical current of a HTS with magnetic field (see Figure 5) confirms that at a temperature of 30 K, the critical current maintains a substantial margin, ensuring the safety of HTS conductors. Consequently, it can be concluded that Type I demonstrates the most substantial safety margin for the SC.

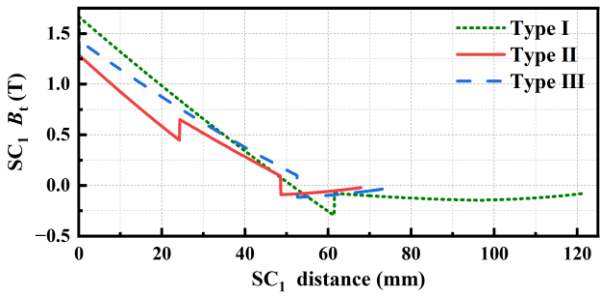

Fig. 18 Comparison of magnetic field of perpendicular SC_1

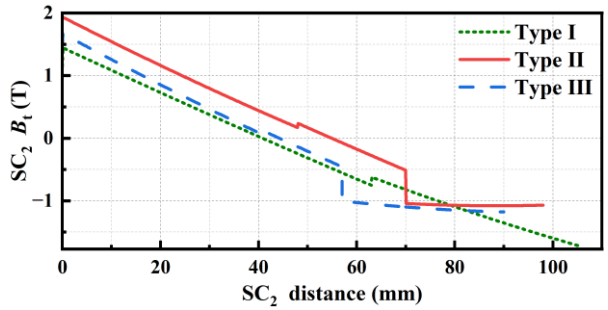

Fig. 19 Comparison of magnetic field of perpendicular SC_2

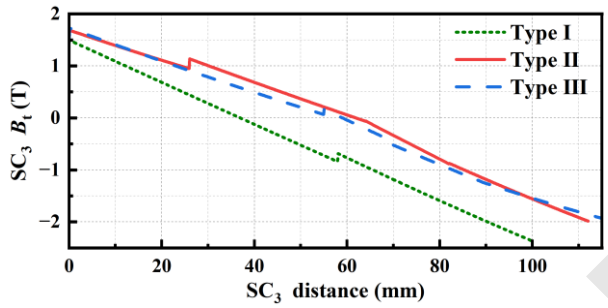

Fig. 20 Comparison of magnetic field of perpendicular SC_3

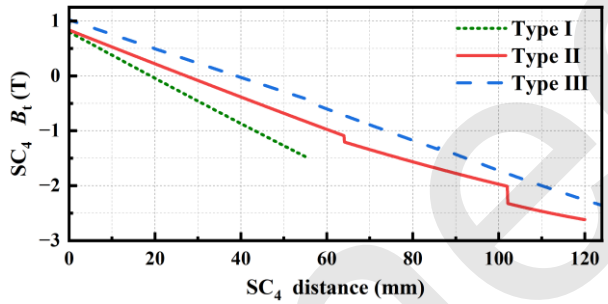

Fig. 21 Comparison of magnetic field of perpendicular SC_4

In a rotating machine, the interaction between the rotor and the stator is primarily decided by the radial component of the magnetic field generated by the rotor. Consequently, the distribution of the radial magnetic induction intensity produced by the SC is crucial.

As shown in Fig. 22, the *R*=550 mm air-gap radial magnetic fields at the same position in Types I and III agree well with one another. The peak of Type III was calculated to be 1.78 T, which is approximately 11% and 9.6% higher than Types I and II, respectively. The corresponding spectra results are shown in Fig. 23. In accordance with the aforementioned design specifications, all three Types consistently maintain a primary magnetic field of 1.38T. It is notable that only the third harmonic components exhibit substantial amplitudes, calculated as 0.233 T, 0.393 T, and 0.225 T for the three Types.

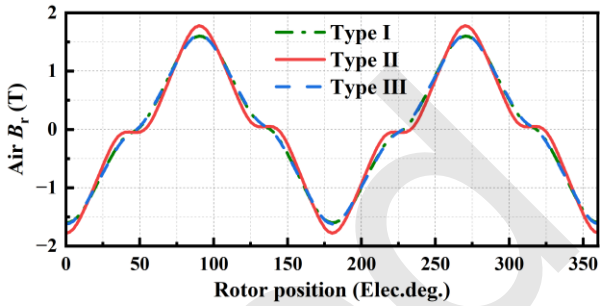

Fig. 22 Comparison of air-gap radial magnetic field

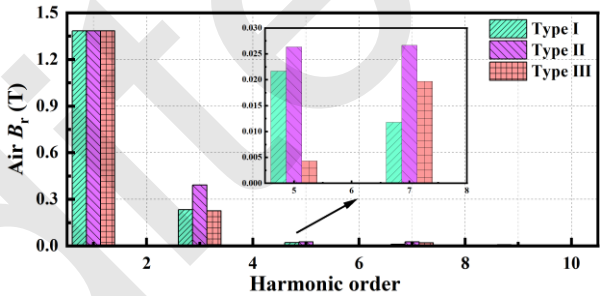

Fig. 23 Comparison of air magnetic-field spectra

The *R*=550 mm tangential component of the magnetic field generated by the rotor is the main cause of vibration noise in a rotating machine. Therefore, attention is also paid to the distribution of tangential magnetic induction intensity generated by the SC. As illustrated in Fig. 24, many peaks are apparent in the Type II curves. The peak of Type III was calculated to be 0.95T, which is approximately 15.8% and 15.1% higher than Types II and III, respectively. As shown in Fig. 25, the spatial distribution of the three Types are non-sinusoidal. Types I and III produced almost the same results, with the highest content in Type III being 0.381T.

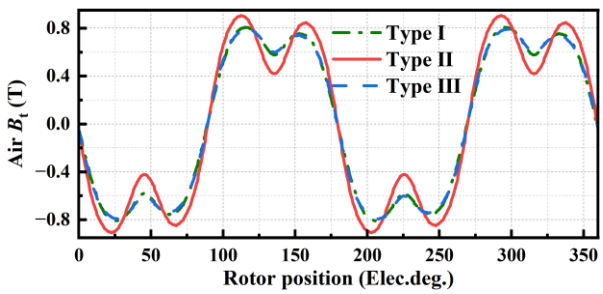

Fig. 24 Comparison of air-gap tangential magnetic field

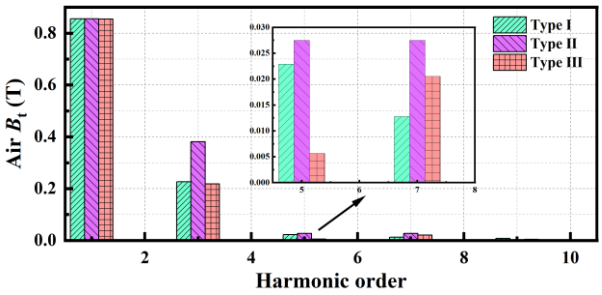

Fig. 25 Comparison of air-gap tangential magnetic-field spectra

The self and mutual inductance of the three Types of HVHTS machines, as determined by 2D finite-element analysis, are presented in Figs. 26 and 28. Fig.24 demonstrates that the mutual inductance amplitude of the three Types of field windings and stator windings A (MLFS) is equal; i.e., the stator and rotor magnetic coupling are equal, meeting the previously outlined design requirements for HVHTS machines. Each pole field-winding self-inductance (LField) for Type III was calculated to be 3.237 H, which is approximately 17.8% and 1.3% higher than for Types I and II, respectively. The mutual inductance of the superconducting field windings of neighboring poles (MLfield) of Type III was calculated to be 421 mH, which is approximately 10.7% and 21.3% higher than for Types I and II, respectively. As can be seen from Figure 25, the maximum mutual inductance within the SC of Type I is 322 mH between SC_2 and SC_3 (Lsc23). In contrast, the maximum mutual inductance within the Type II and Type III coils is 435 mH and 494 mH, respectively, both occurring between SC_3 and SC_4 (Lsc34). Increasing the inductance is detrimental to the ability of a machine to rapidly respond to frequent changes in load by adjusting the field current, thereby weakening its transient regulation capability.

Based on 3D finite-element analysis, the correlation between the three 3D finite-element types closely aligns with the 2D results, predominantly due to a significant enhancement in the 3D outcomes when factoring in the stator-rotor ends. The results reveal that the mutual inductance among the SCs is minimal, indicating a low level of magnetic coupling between them. This means that there is negligible leakage inductance in the field coil (Figure 27 and Figure 30).

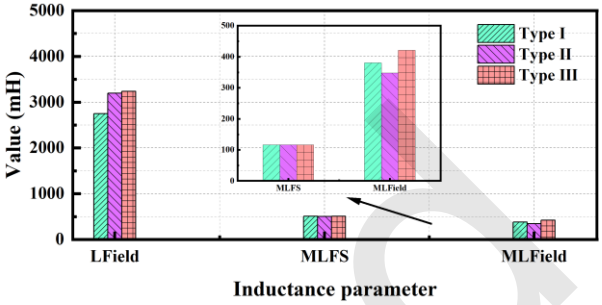

Fig. 26 Comparison of field-coil self and mutual inductance(2D)

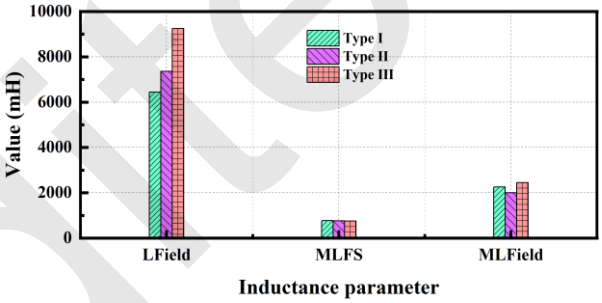

Fig. 27 Comparison of field-coil self and mutual inductance(3D)

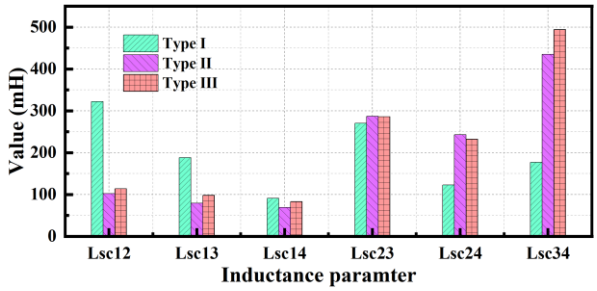

Fig. 28 Comparison of field-coil mutual inductance (2D)

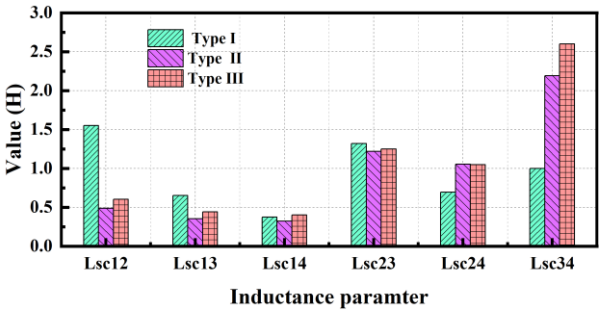

Fig. 29 Comparison of field-coil mutual inductance (3D)

4 Parameter optimization

The findings described in the sections above made it clear that Type I should be considered a promising topology. In this section, we discuss the influence of variations in structural parameters on electromagnetic performance, utilizing the FEM. In order to ensure fairness in the optimization process, we took into account the constraints of equal machine volume, stator heat-dissipation power, and the number of SCs.

4.1 Stator back iron

The HVHTS machines incorporate a stator back iron made of laminated iron. The laminated iron shield has the added benefits of reduced energy loss and the potential to serve as a portion of the stator-winding support structure.

Figure 30 shows the variation in torque and torque ripple with stator environmental shielding thickness. We found that the torque increases and torque ripple decreases immediately when the stator environmental shielding thickness is less than 200 mm. This is because thicker environmental shielding results in a more effective magnetic circuit. Upon achieving a steady state, neither average torque nor torque ripple show a noticeable change when the stator environmental shielding thickness is increased by up to 220 mm. We therefore selected an environmental shielding thickness of 220 mm.

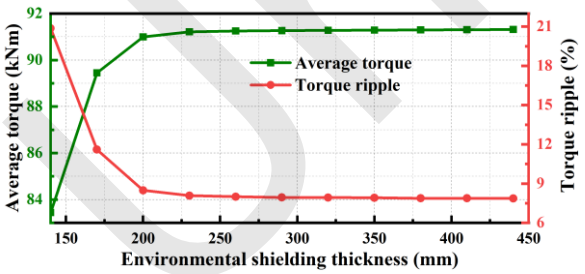

Fig. 30 Comparison of average torque and torque ripple with different back-iron thickness

4.2 The damper shield

The damper shield is a distinctive structure of superconducting machines, which protects the superconducting windings from the impact of higher harmonic originating from the stator side. As illustrated in Fig. 31, many peaks are apparent in the curves of a damper shield with a thickness of 13 mm. Moreover, the torque for a damper-shield thickness of 13 mm peaks at 91.46 kNm, in contrast to the minimum value (calculated at 90.9 kNm) resulting in a torque fluctuation of approximately 0.56 kNm. The power output does not show obvious variation, and the torque ripple is significantly reduced with the increase in shield thickness. We therefore determined that the optimal value of damper-shield thickness was 40 mm. The shield-eddy current losses for the three cases are 30.4 W, 51.0 W and 218.2 W. It should be noted that the shield here includes Dewar's, and a sufficiently thick shield is necessary for effective protection of the superconducting coils under motor transients.

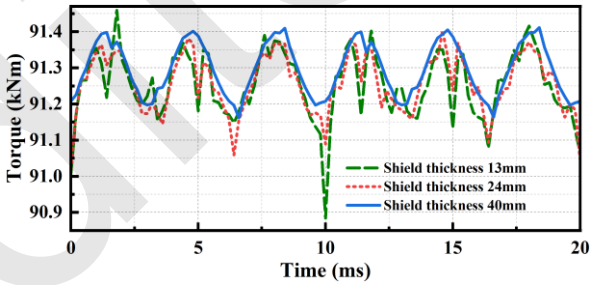

Fig. 31 Comparison of average torque vs shield thickness

4.3 HTS coil

The field winding was thus optimized to meet the low total harmonic distortion of the voltage required by the grid. For a more sinusoidal air-gap magnetic-field waveform, the rotor employs four pairs of double-pancake SCs arranged in a stepped/tiered formation. Ensuring air-gap magnetic-field performance and minimizing the costs of superconducting materials are critical factors for optimization of HVHTS machines. In addition, it is necessary to consider the properties of superconducting materials and design the structure of the SC to weaken the influence of sensitive angle fields on critical current and improve utilization of the superconducting material.

As illustrated in Figure 1, "*b*" denotes the vertical pitch between the trapezoidal superconducting field coils of the rotor. It is presumed that the vertical spacing remains consistent for each coil. As can be

seen in Fig.32, the average torque and torque ripple exhibit an almost linear response to the *b* pitch, owing to the proximity of the SC to the stator. However, the SC must be securely positioned between the structures, necessitating a suitable distance between them. Therefore, it is essential to ensure that the spacing between the coils, denoted as "*b*", is not overly compact. The optimal value of *b* pitch was determined to be 5 mm.

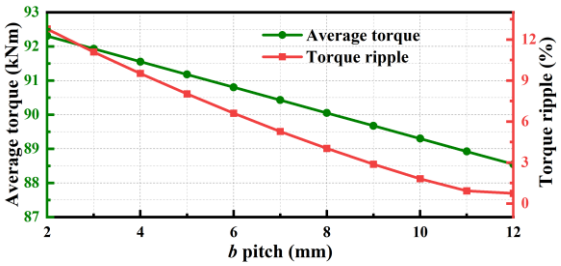

Fig. 32 Comparison of average torque and torque ripple vs *b* pitch

The a_1-a_4 are defined as the inner diameters of the four double-pancake HTS coils. Figs.33 to 36 show that the average torque increases positively with the pitch for a_1, a_2, a_3, and a_4. Ideally, maximizing the value of a_1 among the four horizontal distance variables would yield the highest torque-lifting efficiency, due to the linear decrease in the distance from the stator. However, the torque ripple will be considerably boosted as a_1 pitch increases. With a value of 120 mm for a_1, the torque ripple reaches a substantial 22%. The torque ripple decreases with a_2 pitch first, then reaches a minimum value and increases linearly from 2% to 9%. As the a_3 pitch increases from 160 mm to 380 mm, the torque ripple first drops and then increases linearly from 1.5% to 9%. It is evident that when the a_4 pitch increases, the torque ripple increases slightly, then decreases sharply at the a_4 pitch of 500 mm.

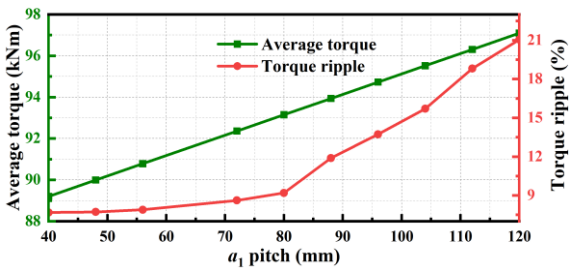

Fig. 33 Comparison of average torque and torque ripple vs a_1 pitch

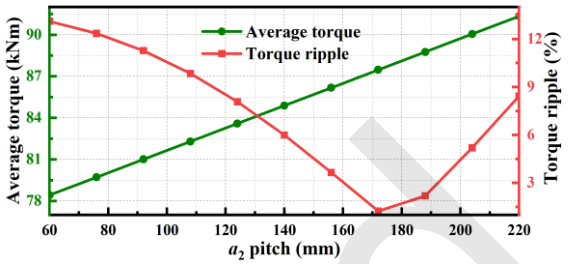

Fig. 34 Comparison of average torque and torque ripple vs a_2 pitch

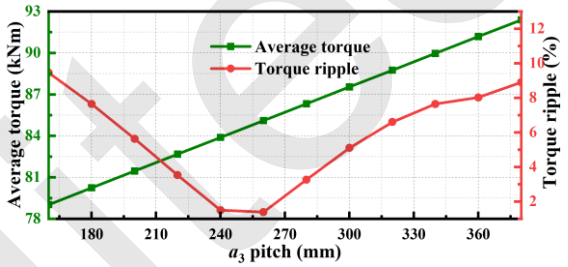

Fig. 35 Comparison of average torque and torque ripple vs a_3 pitch

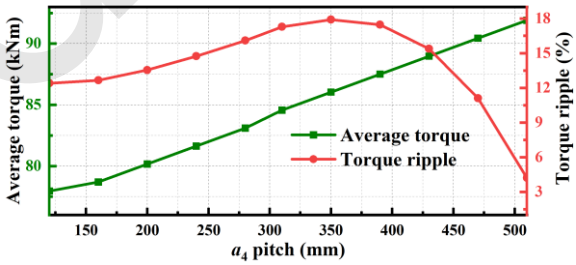

Fig. 36 Comparison of average torque and torque ripple vs a_4 pitch

5 Conclusions

We propose a rated voltage of 35 kV in a DC-field superconducting HVHTS machine . In our model, the machine is considered to be applied in a 35 kV power grid, eliminating the utilization of transformers. Three candidates Types are compared to discuss the tradeoff between the multi-group superconducting field-winding arrangement and machine performances. In addition, we propose an inverted trapezoidal field winding, which experiences the smallest external magnetic field at merely 3.8 T. The number of SCs in the candidate Type is 1840, which is 92.4% and 90.8% of the number for the other two

types. In addition, the THD of the voltage waveform is calculated to be less than 5.1%.The orientation of the strongest magnetic fields in the most promising candidate is predominantly parallel to the SC, which also indicates the most substantial safety margin for the SC. The peak of Type III is calculated to be 0.95T, approximately 15.8% and 15.1% higher than the peaks for Type II and Type III, respectively. Thus, the results reveal that the mutual inductance among the SCs is minimal, signifying a low level of magnetic coupling between them; this indicates negligible leakage inductance in the field coil.

Acknowledgments

This work was supported by State Grid Corporation of China R&D Project (SGTYHT/21-JS-223) and National Natural Science Foundation of China (52293424).

Author contributions

Jien Ma designed the research. Chao Luo processed the corresponding data and wrote the first draft of the manuscript. Bowen Xu, Jiancheng Zhang and Jiabo Shou helped to organize the manuscript. Youtong Fang revised and edited the final version.

Conflict of interest

Chao Luo, Jien Ma, Jiancheng Zhang, Jiabo Shou, Yuan Hu and Youtong Fang declare that they have no conflict of interest.

References

Abrahamsen AB, Mijatovic N, Seiler E, et al., 2009. Design study of 10 kw superconducting generator for wind turbine applications. *IEEE Transactions on Applied Superconductivity*, 19(3):1678-1682. https://doi.org/10.1109/TASC.2009.2017697

Balachandran T, Yoon A, Lee D, et al., 2022. Ultrahigh-field, high-efficiency superconducting machines for offshore wind turbines. *IEEE Transactions on Magnetics*, 58(2):1-5. https://doi.org/10.1109/TMAG.2021.3094163

Bong U, An S, Voccio J, et al., 2019. A design study on 40 mw synchronous motor with no-insulation hts field winding. *IEEE Transactions on Applied Superconductivity*, 29(5):1-6. https://doi.org/10.1109/TASC.2019.2908548

Cucciniello N, Lee D, Feng HY, et al., 2022. Superconducting niobium nitride: A perspective from processing, microstructure, and superconducting property for single photon detectors. *Journal of Physics-Condensed Matter*, 34(37):374003. https://doi.org/10.1088/1361-648X/ac7dd6

Dias FJM, Sotelo GG, Júnior RDA, 2022. Performance comparison of superconducting machines with induction motors. *IEEE Trans. Appl. Supercond.*, 32(7):1-5. https://doi.org/10.1109/TASC.2022.3188461

Duan X, Shi Z, Song M, et al., 2022. Application prospects of the superconducting dynamic synchronous condenser. *IEEE Transactions on Applied Superconductivity*, 32(6):1-5. https://doi.org/10.1109/TASC.2022.3168497

Fang K, Qiu L-M, Jiang X, et al., 2015. Temperature inhomogeneity in high capacity pulse tube cryocoolers. *Journal of Zhejiang University-SCIENCE A*, 16(11):910-921. https://doi.org/10.1631/jzus.A1400296

Gao C, He D, Zhou Y, et al., 2019. A study on the space charge characteristics of ac sliced xlpe cables. *IEEE Access*, 7:20531-20537. https://doi.org/10.1109/ACCESS.2019.2893604

Hao L, Sun Y, Qiu A, et al., 2012. Steady-state calculation and online monitoring of interturn short circuit of field windings in synchronous machines. *IEEE Transactions on Energy Conversion*, 27(1):128-138. https://doi.org/10.1109/TEC.2011.2169264

Hsieh M-F, Lin C-K, Lin I-H, 2013. Design and analysis of high temperature superconducting generator for offshore wind turbines. *Ieee Transactions on Magnetics*, 49(5):1881-1884. https://doi.org/10.1109/TMAG.2013.2246146

Kim Y, Hempstead C, Strnad A, 1964. Resistive states of hard superconductors. *Reviews of Modern Physics*, 36(1P1):43-&. https://doi.org/10.1103/RevModPhys.36.43

Komiya M, Aikawa T, Sasa H, et al., 2019. Design study of 10 mw rebco fully superconducting synchronous generator for electric aircraft. *IEEE Transactions on Applied Superconductivity*, 29(5):1-6. https://doi.org/10.1109/TASC.2019.2906655

Komiya M, Sugouchi R, Sasa H, et al., 2020. Conceptual design and numerical analysis of 10 mw fully superconducting synchronous generators installed with a novel casing structure. *IEEE Transactions on Applied Superconductivity*, 30(4):1-7. https://doi.org/10.1109/TASC.2020.2989746

Kovalev K, Ivanov N, Tulinova E, et al., 2019. Methodic of calculation of fully hts salient-pole electrical machine. *Przeglad Elektrotechniczny*, 95(1):213-218. https://doi.org/10.15199/48.2019.01.51

Lee S-B, Lee T-H, Jung E-H, et al., 2014. Development of 250kv hvdc xlpe cable system in korea. Proc Int Symp Electr Insul Mater, p.334-337. https://doi.org/10.1109/ISEIM.2014.6870787

Li Y, Qiu L, Zhi Y, et al., 2023. An overview of bearing voltages and currents in rail transportation traction motors. *Journal of Zhejiang University-SCIENCE A*, 24(3):226-242. https://doi.org/10.1631/jzus.A2200180

Liu X, Wang Y, Luo X, et al., 2022. Stator single-line-to-ground fault protection for powerformers based on hsgc and cnn. *Frontiers in Energy Research*, 10:998797. https://doi.org/10.3389/fenrg.2022.998797

Liu Y, Grilli F, Cao J, et al., 2021. An electromagnetic design of a fully superconducting generator for wind application. 14(22):7811.

Manolopoulos CD, Iacchetti MF, Smith AC, et al., 2020. Comparison between coreless and yokeless stator designs

in fully-superconducting propulsion motors. *IEEE Trans. Appl. Supercond.*, 30(6):1-7. https://doi.org/10.1109/TASC.2020.2992588

Masson PJ, Luongo CA, 2005. High power density superconducting motor for all-electric aircraft propulsion. *IEEE Trans. Appl. Supercond.*, 15(2):2226-2229. https://doi.org/10.1109/TASC.2005.849618

Metwally IA, Radwan RM, Abou-Elyazied AM, 2008. Powerformers: A breakthrough of high-voltage power generators. *IEEE Potentials*, 27(3):37-44. https://doi.org/10.1109/MPOT.2008.915315

Miller T, Hughes A, 1977. Comparative design and performance analysis of air-cored and iron-cored synchronous machines. *Proceedings of the Institution of Electrical Engineers-London*, 124(2):127-132. https://doi.org/10.1049/piee.1977.0022

Muttaqi KM, Islam R, Sutanto D, 2019. Future power distribution grids: Integration of renewable energy, energy storage, electric vehicles, superconductor, and magnetic bus. *IEEE Transactions on Applied Superconductivity*, 29(2):3800305. https://doi.org/10.1109/TASC.2019.2895528

Oishi I, Nishijima K, 2002. Summary of development of 70 mw class model superconducting generator—research and development of superconducting for electric power application. *Cryogenics*, 42(3):157-167. https://doi.org/10.1016/S0011-2275(02)00032-2

Perers R, Lundin U, Leijon M, 2007. Development of synchronous generators for swedish hydropower: A review. *Renew. Sust. Energ. Rev.*, 11(5):1008-1017. https://doi.org/10.1016/j.rser.2005.07.007

Qiuli SE, 2022. Multi-scale nonlinear stress analysis of nb3sn superconducting accelerator magnets. *Superconductor Science & Technology*, (4):35. https://doi.org/10.1088/1361-6668/ac5a11

Seo K, Yoon J, Cha J, et al., 2023. Design optimization of hts field coils for high power density motors based on continuum sensitivity analysis. IEEE Transactions on Applied Superconductivity, 33(5):1-5. https://doi.org/10.1109/TASC.2023.3268146

Sumption MD, Murphy J, Susner M, et al., 2020. Performance metrics of electrical conductors for aerospace cryogenic motors, generators, and transmission cables. *Cryogenics*, 111:103171. https://doi.org/https://doi.org/10.1016/j.cryogenics.2020.103171

Terao Y, Seta A, Ohsaki H, et al., 2019. Lightweight design of fully superconducting motors for electrical aircraft propulsion systems. *IEEE Trans. Appl. Supercond.*, 29(5):1-5. https://doi.org/10.1109/TASC.2019.2902323

Tian Q, Lin X, 2006. A new novel differential protection scheme for a high-voltage, cable-wound generator. IEEE PES Transm. Distrib. Conf. Expo.: Latin America, TDC, p.1-6. https://doi.org/10.1109/TDCLA.2006.311625

Wang L, Lien S-Y, Prokhorov AV, 2015. Stability improvement of a large-scale offshore wind farm using a superconducting magnetic energy-storage unit and a superconducting fault-current limiter. IEEE Ind. Appl. Soc. Annu. Meet., IAS - Conf. Rec., p.1-7. https://doi.org/10.1109/IAS.2015.7356927

中文概要

题　目：35 kV 高压高温超导同步电机设计与励磁绕组优化

作　者：罗超[1]，许博文[1]，马吉恩[1]，张建承[2]，寿佳波[1]，胡源[1]，方攸同[1]

机　构：[1]浙江大学，电气工程学院，中国杭州，310027；[2]国网浙江省电力有限公司电力科学研究院，中国杭州，310014

目　的：目前国内外采用的技术路线均为传统调相机的超导化，即仅仅应用超导转子对传统常导转子进行简单替换，超导调相机的优势未能完全发挥。例如：国内外已经投运的超导调相机均采用 10 kV 以下端电压，必须通过升压变压器与电网连接。本文基于超导电机强磁场、大气隙的优势，提出了高压定子电缆绕组在超导电机中的应用。

创新点：1. 利用交联聚乙烯电缆绕组实现直流励磁型超导电机 35kv 的额定电压，将摒弃升压变压器进一步提高超导电机系统的功率密度；2. 在 35kv 额定电压条件下，提出新型倒梯形超导磁场绕组排列方式，实现最少超导材料用量，小转矩脉动和小总谐波畸变率。

方　法：1. 通过理论分析计算，结合电机电磁性能得到应用于 35kV 超高压超导电机的交联聚乙烯电缆绕组尺寸及规格；2. 通过有限元分析，证明所设计的高压高温超导电机不仅满足 35kV 额定电压的要求，而且漏磁、转矩波动和谐波畸变很小，验证了超高压超导电机的可行性；3.研究比较三种候选类型超高压超导电机，讨论了多组超导场绕组布置与电机性能之间的关系，在此基础上，通过仿真证明倒梯形超导磁场绕组具有超导材料用量最小、超导安全余量最大、转矩脉动小、总谐波畸变小的优点。

结　论：1. 优化后的 35 kV 超高压超导调相机电磁性能优异，保证额定电压的同时，漏磁和转矩波动等都很小，可以用于直连电网而不需要变压器，并且可以实现更高的端电压；2. 倒梯形励磁绕组排列被选择，其外加磁场最小，仅为 3.8T，超导线圈匝数最小 1840，分别为其他两种绕组的 92.4%和 90.8%；3. 优化后的超高压超导电机电压波形的 THD 小于 0.3%。同时，强磁场的方向基本与超导线圈平行，这意味着优化后的电机安全裕度最大。

关键词：超导电机；高压定子电缆绕组；倒置型励磁绕组；谐波失真率